



Regular Article

Structures of the troponin core domain containing the cardiomyopathy-causing mutants studied by small-angle X-ray scattering

Tatsuhito Matsuo¹, Soichi Takeda², Toshiro Oda^{3,4} and Satoru Fujiwara¹

¹Quantum Beam Science Center, Japan Atomic Energy Agency, Tokai-mura, Naka-gun, Ibaraki 319-1195, Japan

²National Cerebral and Cardiovascular Center Research Institute, Suita, Osaka 565-8565, Japan

³RIKEN SPring-8 center, RIKEN Harima Institute, Sayo, Hyogo 679-5148, Japan

⁴Present address: Tokai Gakuin University, Kagamihara, Gifu, 504-8511, Japan

Received September 28, 2015; accepted December 1, 2015

Troponin (Tn), consisting of three subunits, TnC, TnI, and TnT, is a protein in the thin filaments in muscle, and, together with another thin-filament protein tropomyosin (Tm), plays a major role in regulation of muscle contraction. Various mutations of Tn cause familial hypertrophic cardiomyopathy. These mutations are directly related to aberrations in this regulatory mechanism. Here we focus on the mutations E244D and K247R of TnT, which reside in the middle of the pathway of the Ca²⁺-binding signal from TnC to Tm. These mutations induce an increase in the maximum tension of cardiac muscle without changes in Ca²⁺-sensitivity. As a first step toward elucidating the molecular mechanism underlying this functional aberration, we carried out small-angle X-ray scattering experiments on the Tn core domain containing the wild type subunits and those containing the mutant TnT in the absence and presence of Ca²⁺. Changes in the overall shape induced by the mutations were detected for the first time by the changes in the radius of gyration and the maximum dimension between the wild type and the mutants. Analysis of the scattering curves by model calculations shows that TnC adopts a dumbbell structure regardless of the mutations, and that the mutations change the distributions of the conformational ensembles so that the flexible N- and C-terminal regions of TnT become close to the center of the whole molecule. This suggests, since these regions are related to the Tn-Tm interactions, that

alteration of the Tn-Tm interactions induced by the mutations causes the functional aberration.

Key words: muscle regulatory proteins, solution scattering, genetic algorithm, missense mutation

Troponin (Tn) is a protein complex consisting of three subunits, TnC, TnI, and TnT. This protein complex, which resides in the thin filaments in muscle, plays a major role in the Ca²⁺-sensitive regulation of muscle contraction in vertebrate skeletal and cardiac muscles [1,2]. When the concentration of Ca²⁺ increases in muscle cells, Ca²⁺ binds to one of the Tn-subunits, TnC. This triggers a series of structural changes of TnC, TnI, TnT, and another regulatory protein in the thin filaments, tropomyosin (Tm). This releases inhibition of the interaction between actin in the thin filaments and myosin in the thick filaments. This acto-myosin interaction causes sliding of the thick and thin filaments past each other, and thus muscle contraction occurs.

Various mutations in Tn are known to cause various types of cardiomyopathy [3,4]. Mutations at various sites along the pathway of the Ca²⁺-binding signal from TnC to Tm cause various effects on the regulatory function. Functional analysis of cardiomyopathy-causing mutants of Tn showed that the aberrations caused by these mutations are classified into three types: the increase in Ca²⁺-sensitivity (type I), the decrease in Ca²⁺-sensitivity (type II), and the increase in the maximum tension without alteration of Ca²⁺-sensitivity (type III) [3,5]. Most of the mutations are located in the regions directly related to the regulatory function such as the Ca²⁺-

Corresponding author: Satoru Fujiwara, Quantum Beam Science Center, Japan Atomic Energy Agency, 2-4 Shirakata-Shirane, Tokai-mura, Naka-gun, Ibaraki 319-1195, Japan.
e-mail: fujiwara.satoru@jaea.go.jp

binding region in TnC, the C-terminal region of TnI containing the inhibitory region that interacts with TnC and the actin-binding region, and the Tm-binding regions of TnT. These mutations cause the type I or the type II aberrations. On the other hand, there are two mutations, located in the region not directly involved with the regulatory function. The mutations E244D and K247R in TnT are located in the coiled-coil region formed by TnI and TnT (the IT arm [6]) of the Tn core domain. These mutations cause the type-III aberration [7,8]. Since this IT arm connects the region containing the Ca²⁺-binding site of TnC and the Tm-binding region of TnT, this region may play a pivotal role related to propagation of the Ca²⁺-binding signal from TnC to Tm. Elucidation of the effects of these mutations should thus provide insights into not only the mechanism of the type-III aberration but also the mechanism of the propagation of the Ca²⁺-binding signal.

For elucidation of the effects of the mutations, it is important to investigate how the structure of Tn may be changed by the mutations. Crystal structure analysis of proteins provides structures in atomic detail. Crystal structure analysis of the human cardiac (hc) Tn core domain, consisting of the full-length TnC, TnI with the 30 residues at the N-terminal region deleted, and TnT2 (the residues 183–288 of TnT), showed, however, that the Tn core domain is a flexible molecule [6]. Crystal-packing force may distort the structure in crystals. The structure of the hcTn core domain in solution, in which such extra forces do not exist, should therefore be investigated.

Small-angle scattering (SAS) is a method suitable to investigate structures of proteins and protein complexes in solution. SAS is sensitive to structural changes as well as association states though it is a low-resolution method. There are indeed various structural studies on Tn-related protein complexes using small-angle neutrons scattering (SANS) and small-angle X-ray scattering (SAXS) [9–15]. SANS, combined with selective deuteration and the contrast matching, provides information on individual subunits in protein complexes, which cannot be available from SAXS. On the other hand, SAXS measurements, by using synchrotron radiation facilities, can be carried out at lower sample concentrations and smaller sample volume than those required for SANS measurements. These characteristics of SAXS are advantageous for samples available only with low yield. In addition, measurements at low sample concentrations suffer less effects of inter-particle interference. Analysis of SAXS curves using various modeling techniques provides low-resolution models of proteins and protein complexes [16]. Here, we employed SAXS to investigate the structures of the hcTn core domain. The SAXS measurements on the hcTn core domain containing native subunits and that containing mutant TnT (K247R or E244D) detected structural changes induced by these mutations. Analysis by model calculations showed that the mutations induce changes in the distribution of the conformational ensembles.

Materials and Methods

Sample preparations

All subunits of Tn used in this study were cysteineless and expressed in *E. coli* BL21(DE3)-pLys-S as described [8]. Each subunit was purified separately. Purification of TnI and TnC was done as described [8]. TnT with His-tag at the N-terminus was purified by a series of chromatography using HiTrap SP FF (GE Healthcare, Pittsburgh, PA), HisTrap FF crude (GE healthcare, Pittsburgh, PA), and RESOURCE RPC (GE Healthcare, Pittsburgh, PA). Note that the His-tag was not removed. These purified subunits were reconstituted into the Tn core domain (the molecular mass of 52 kDa), as described [17]. The reconstituted complexes were further purified by gel filtration using the column Superdex 200 10/300 GL (GE Healthcare, Pittsburgh, PA) in solution containing 50 mM HEPES (pH 8.0), 0.5 M NaCl, 5 mM MgCl₂, and 1 mM dithiothreitol, just before the SAXS experiments. Preparation of the samples in the absence of Ca²⁺ was done by adding EGTA to the final concentration of 5 mM. This made the concentration of free Mg²⁺ 1.8 mM. Preparation of the samples in the presence of Ca²⁺ was done by adding CaCl₂ to the final concentration of 5 mM. These sample solutions were concentrated to appropriate protein concentrations for the SAXS experiments.

Bovine serum albumin, purchased from Wako Pure Chemical Industries, Ltd. (Osaka, Japan), was purified by gel-filtration using the same column as above just before the SAXS experiments. The eluted sample solution at the concentration of 2.6 mg/ml was used as a sample.

Small-angle X-ray scattering experiments

The SAXS experiments were carried out on the beam line BL45XU-SAXS [18] at SPring-8, Hyogo, Japan, using incident X-rays of $\lambda=0.9 \text{ \AA}$ at a sample-to-detector distance of 2.4 m. Scattering profiles were collected using a cooled CCD equipped with an X-ray image intensifier [19]. Exposure time for each sample was 1 s. Checking the changes in the profiles with increasing exposure time confirmed that no radiation damage occurred during this exposure time. All the measurements were done at 10.0°C. The net scattering profile of each sample was obtained by subtracting the scattering profile of the buffer from that of the sample, scaled by the intensity of the incident beam measured by the ion chamber placed upstream of the sample position. The profile was then circularly averaged to obtain the one-dimensional scattering curve.

Guinier analysis

The scattering curves obtained were analyzed using the Guinier plots. In the small-angle region, the scattering curve, $I(Q)$, can be approximated by the equation,

$$I(Q) = I(0) \exp(-R_g^2 Q^2/3), \quad (1)$$

where Q is the momentum transfer ($Q=4\pi\sin\theta/\lambda$, where 2θ

is the scattering angle, and λ is the wavelength of the incident X-ray), $I(0)$ is the scattering intensity at $Q=0$, and R_g is the radius of gyration. The plot of $\ln I(Q)$ against Q^2 (the Guinier plot), is thus fit by a straight line [20]. The slope of the linear fit provides the value of R_g , and the molecular weight of a particle of interest can be estimated from the $I(0)$ value.

Model calculations

Analysis of the overall shape of the Tn core domain was carried out by model calculations as follows: (1) a model based on the crystal structure was constructed for structural refinement, (2) several pivot points were selected in this model, (3) starting models were generated by random rotation around the pivot points, and (4) the structural search by the rigid body refinement was carried out. The steps (3) and (4) were repeated so that ensembles of the structures fit to the scattering curves were obtained. Each step in this model calculation is described below.

Construction of a model based on the crystal structure

An atomic model of the Tn core domain was constructed from the structure obtained from the analysis of new crystals of the hcTn core domain (PDB accession number: 4Y99), which were obtained under the different crystallizing conditions from the “old” structure (PDB accession number: 1J1E, Ref. 6). The overall structure obtained from this new crystal is very similar to the old structure (1J1E) except for the position of the N-terminal region of TnT. This new structure is shown in Figure 1 as an example of the starting models for structural search. Details of the new crystal structure analysis will be described elsewhere (in preparation). The missing residues in this crystal structure (the residues 86–90 in TnC, 183–198 and 272–288 in TnT, and 31–42, 138–147, and 167–210 in TnI) were also similar to those in the 1J1E structure. The missing terminal regions in TnI and TnT (TnI_{31–42}, TnI_{167–210}, TnT_{183–198}, and TnT_{272–288}) were complemented as loop structures using the program RanCh [21], and the missing residues connecting two separate regions in TnI (TnI_{138–147}) were also complemented as loop structures using a template-based loop structure prediction server ArchPRED [22].

Selection of the pivot points

In the model thus constructed, the pivot points, around which the structures can rotate freely, were set around the central region in the IT arm (Gly⁹¹ (TnC), Ser⁴² (TnI), Gly¹³⁷ (TnI), His²²³ (TnT), and Gln²⁷² (TnT) shown in Fig. 1). These pivot points were selected according to the following facts: crystal structure analysis of the hcTn core domain showed that the structure is flexible at the regions connecting the IT arm and the regulatory head region, which include the residues Gly⁹¹ (TnC), Ser⁴² (TnI), Gly¹³⁷ (TnI), and Gln²⁷² (TnT) [6]; the difference between the 1J1E structure and the structure employed here is only in the N-terminal region of TnT (the region between the N-terminus and the residues around

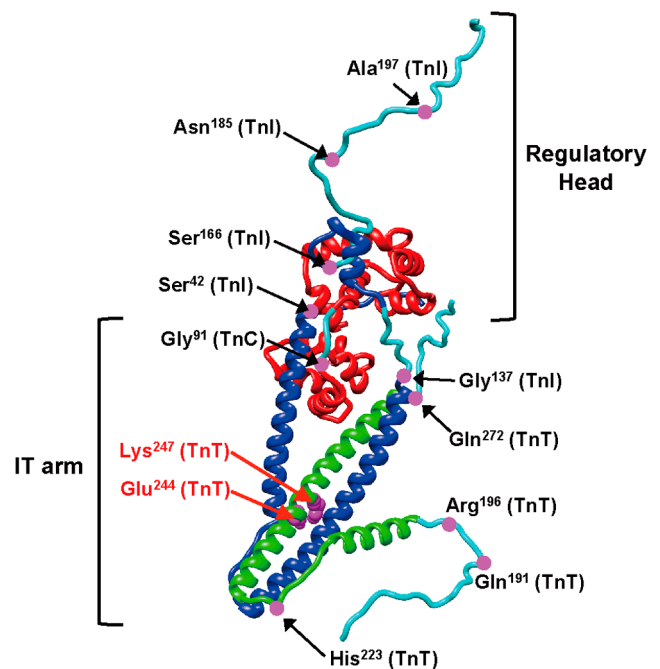


Figure 1 Ribbon representation of an example of the starting models of the Tn core domain based on the crystal structure. TnC, TnI, and TnT are highlighted in red, blue, and green, respectively. In this crystal structure, the residues 86–90 in TnC, the residues 183–198 and 272–288 in TnT, and the residues 138–147, and 167–210 in TnI, are missing. These missing residues, which are complemented as loop structures, are shown in cyan. Note that the residues corresponding to the extra 12 residues of His-tag at the N-terminus of TnT, are added in addition to the residues 183–198 in TnT. The pivot points for free rotation are marked by filled circles in magenta. The movable regions are the residues 183–223 of TnT (containing the extra 12 residues of His-tag), 272–288 of TnT, 31–42 of TnI, 137–210 of TnI, and the N-lobe of TnC. The positions of the mutations (Glu²⁴⁴ and Lys²⁴⁷) are also shown in the diagram. The diagram is drawn using UCSF Chimera [59].

His²²³); and comparison between the crystal structures of the 1J1E structure and the chicken skeletal (cs) Tn core domain (PDB accession number: 1YTZ) showed that the major differences are only in the position of the N-lobe of TnC and the N-terminal region of TnT [23].

Additional pivot points (Ser¹⁶⁶ (TnI), Asn¹⁸⁵ (TnI), Ala¹⁹⁷ (TnI), Gln¹⁹¹ (TnT), Arg¹⁹⁶ (TnT) shown in Fig. 1) were selected to take flexibility of the loop structures into account. The distance between the centers of gravity of the N-lobe and the C-lobe of TnC was also assumed to be varied, taking account of a possibility that TnC adopts an elongated structure as shown by comparison between the 1J1E structure and the 1YTZ structure [23]. The missing residues 86–90 in TnC (TnC_{86–90}), which connect the N- and C-lobes, were thus placed evenly on the line connecting the residues 85 and 91 of TnC. The changes in the distance between the N- and C-lobes of TnC can be described by the changes in the distance between the neighboring residues. In the models of the mutants, the residues Glu²⁴⁴ or Lys²⁴⁷ of TnT were replaced by Asp (E244D) or Arg (K247R), respectively.

Generation of starting models

The starting models were produced by generating randomly the values of the parameters specifying the positions of the movable regions set by the pivot points. The parameters were the Euler angles of rotation around each pivot point and the distance between the N- and C-lobes of TnC. For the models in the presence of Ca^{2+} , an additional constraint was introduced, in which the residues 150–159 of TnI (the switch helix) were attached to the N-lobe of TnC [6]. The N-lobe of TnC and the region containing the switch helix were thus moved as a rigid body.

Structural search

The structural search was carried out by rigid body refinement of the models. The models generated during the search by changing the parameter values defining the positions of the movable regions were evaluated by the residual between the calculated scattering curve of the model and the experimental scattering curve. The scattering curve of the model was calculated using the program CRY SOL [24] with the density of the hydration shell 10% higher than that of bulk water (default setting). The residual, χ^2 , of the calculated scattering curve from the experimental curve was calculated using the equation,

$$\chi^2 = (1/(N_p - n - 1)) \sum_{i=1}^{N_p} ((I_{exp}(Q_i) - kI_{calc}(Q_i))/\sigma_{exp}(Q_i))^2, \quad (2)$$

where N_p is the number of data points, n is the number of the parameters, $I_{exp}(Q_i)$ and $I_{calc}(Q_i)$ are the intensity of the experimental scattering curve and that of the calculated scattering curve of the model at Q_i , respectively, k is the scaling factor determined so that the $I(0)$ values are identical, and $\sigma_{exp}(Q_i)$ is the standard deviation of the experimental scattering curve at Q_i .

The search to find a model with the minimum residual was carried out using a genetic algorithm [25]. In this algorithm, a set of parameter values is called a “gene”. In the first round of calculations (the first generation), 10 genes (corresponding to the starting models) are randomly generated. Out of the 10 models generated from these 10 genes, the 2 genes of the models with the smallest χ^2 are selected, and passed to the next generation. For the genes of the remaining 8 models, two genetic operations, the crossover and the random mutation, are performed, after which they are passed to the next generation. In the crossover, 2 genes are randomly selected out of the 10 genes and the values at an arbitrary position on the genes are exchanged. In the random mutation, one parameter in a gene is randomly changed. In each generation, these operations are repeated. Calculation is terminated when the smallest χ^2 does not change for 100 generations, and the model with the smallest χ^2 is accepted as a final model.

The search was repeated 1000 times for each sample so that an ensemble of the models having the good fits to the experimental scattering curves was obtained. To facilitate

the efficient convergence of the searches, a constraint that the models have the radii of gyration within a range of two standard deviations of the experimental values was also employed.

The model obtained from each search represents one of the possible conformations that are consistent with the experimental SAXS curve. Repeating the search makes it possible to search the large conformational space because each step in the search randomly explores the conformational space. The ensemble of the models obtained from the repeated searches thus provides the distribution of the possible conformations.

Alternative model calculations using the Ensemble Optimization Method

The model calculations described above are based on the assumption that the scattering curves are described by one conformation of the protein that can adopt in solution. For flexible proteins, however, multiple conformations could coexist in solution. Although the repeated searches provide an ensemble of possible conformations, the calculations without taking account of the possible coexistence of multiple conformations may bias the distributions of the conformations. We thus carried out, as an alternative procedure of the model calculations, the model calculation using the Ensemble Optimization Method (EOM), which takes account of the coexistence of different conformations in solution [21]. By comparing the results of the model calculations above and those using the EOM, we checked validity of the model calculations described above.

The EOM produces a set of conformers, the average scattering curve of which is best-fit with the experimental scattering curve. These conformers are selected, using a genetic algorithm, from a pool of a large number of randomly generated models (10,000 models as a default setting). In this study, 10,000 conformations of the Tn core domain were randomly created by the program RanCh from the 4Y99 structure as a template structure with complementing the missing residues. The ensemble of these 10,000 models was used as a conformation pool. The conformation pools of the K247R and E244D mutants were created by replacing the residues 247 and 244 of TnT of each model in the conformation pool of the wild-type Tn with an arginine and asparagine, respectively. Subsequent selection of the best ensemble of the models based on the genetic algorithm was conducted by the program GAJOE [21].

Results

Small-angle X-ray scattering experiments

We prepared the hcTn core domain consisting of full-length TnC, TnI with the 30 residues at the N-terminus deleted, and TnT (the residues 183–288) with the 12 residues of the His-tag attached to the N-terminus. The Tn core domain prepared contained either the wild-type TnT, the

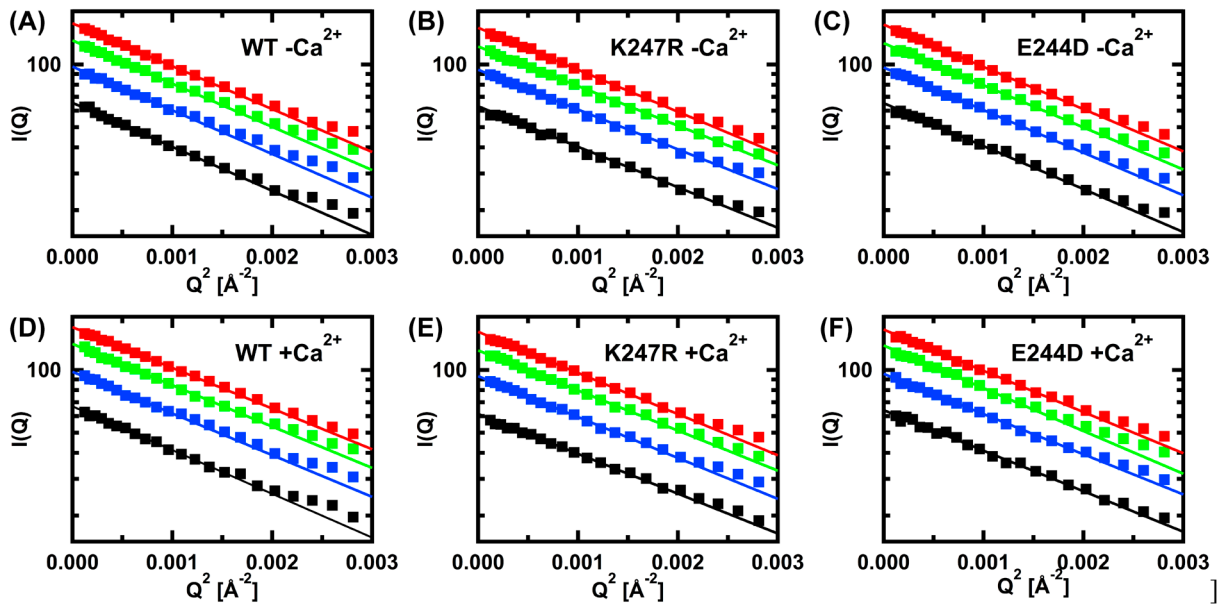


Figure 2 Summary of the Guinier plots of the scattering curves of (A) WT, (B) K247R, and (C) E244D in the $-Ca^{2+}$ state, and (D) WT, (E) K247R, and (F) E244D in the $+Ca^{2+}$ state. The error bars are within symbols. Solid lines are the results of the least-square fit using Eq. 1 to the Q^2 region $\leq 0.001 \text{ \AA}^{-2}$. This maximum Q corresponds to $R_g \cdot Q \sim 1.2$. The concentrations of the proteins are: in (A), 2.1 mg/ml, 1.7 mg/ml, 1.2 mg/ml, and 0.79 mg/ml from top to bottom; in (B), 2.0 mg/ml, 1.7 mg/ml, 1.2 mg/ml, and 0.70 mg/ml from top to bottom; in (C), 2.1 mg/ml, 1.7 mg/ml, 1.2 mg/ml, and 1.0 mg/ml from top to bottom; in (D), 2.1 mg/ml, 1.7 mg/ml, 1.2 mg/ml, and 0.86 mg/ml from top to bottom; in (E), 2.0 mg/ml, 1.6 mg/ml, 1.2 mg/ml, and 0.73 mg/ml from top to bottom; and in (F), 2.1 mg/ml, 1.7 mg/ml, 1.2 mg/ml, and 0.93 mg/ml from top to bottom.

K247R mutant of TnT, or the E244D mutant of TnT (termed WT, K247R, and E244D, respectively). The SAXS measurements on these samples were performed at several protein concentrations between 0.7 mg/ml and 2.1 mg/ml in the absence and presence of Ca^{2+} (the $-Ca^{2+}$ and $+Ca^{2+}$ states). The scattering curves obtained were analyzed by the Guinier plots. Figure 2 shows a gallery of the Guinier plots, from which the parameters, R_g and $I(0)$, are evaluated. Note that no upward deviations from the straight lines in the lower Q region are observed, indicating that there is no appreciable aggregation in the samples. Figures 3(A) and 3(B) show the plots of the R_g against the protein concentration. Extrapolation to zero protein concentration provides the R_g values with eliminating the effects of the inter-particle interferences [26,27]. The extrapolated R_g values are summarized in Table 1. The values are different between WT and the mutants though the difference between WT and E244D in the $-Ca^{2+}$ state is within a range of one standard deviation.

Figures 3(C) and 3(D) show the plots of the $I(0)/c$ (where c denotes the concentration of the protein), from which the molecular weights can be estimated, against the protein concentration. Extrapolation of the $I(0)/c$ to $c=0$ converged to similar values regardless of the samples. The molecular weights were estimated by comparing these extrapolated $I(0)/c$ values with that of the protein bovine serum albumin (BSA), which has the molecular weight of 66 kDa. The estimated molecular weights are also summarized in Table 1. The molecular weights are similar in all samples, and the

values themselves are within about a 10% range of the expected molecular weight of 52 kDa of the Tn core domain. This, again, indicates no appreciable aggregation in the samples. The R_g depends on an overall size as well as a shape of a particle. Since the samples measured here are considered to be monomeric, the differences in the R_g indicate that the overall shape change is induced by the mutations.

Figure 4 shows the experimental scattering curves extrapolated to zero protein concentration, in which the effects of the inter-particle interference are minimal, and the corresponding pair-distance distribution functions, $p(r)$, calculated from these extrapolated scattering curves using the program DATGNOM [28]. The maximum dimension D_{max} was estimated from the $p(r)$ function, and the values of the D_{max} obtained are summarized in Table 1. All the $p(r)$ functions show a unimodal shape, indicating that structural integrity is not affected by the mutations. Comparison of the D_{max} values indicates that the mutants adopt more compact shape than WT in the $+Ca^{2+}$ state.

Model Calculations

To analyze the shape changes induced by the mutations, analysis by model calculation was performed. The experimental scattering curves extrapolated to zero protein concentration shown in Figure 4 were used for fitting by the model scattering curves. The whole range of the measured Q (0.013 \AA^{-1} – 0.2 \AA^{-1}) was used in the fits. The residuals of the scattering curves of the models obtained, calculated using

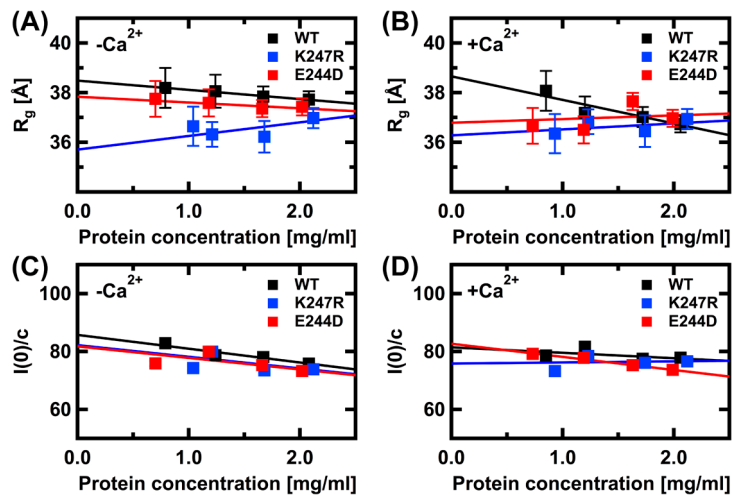


Figure 3 Protein concentration dependence of the R_g and $I(0)/c$ estimated from the Guinier analysis. The concentration dependences of (A) the R_g in the $-Ca^{2+}$ state, (B) the R_g in the $+Ca^{2+}$ state, (C) the $I(0)/c$ in the $-Ca^{2+}$ state, and (D) the $I(0)/c$ in the $+Ca^{2+}$ state are shown.

Table 1 Summary of the radii of gyration, the molecular weights, and the maximum dimension of the particle

		R_g^a (Å)	M.W. ^b (kDa)	D_{max} (Å)
$-Ca^{2+}$	WT	38.5 (1.1)	58 (2)	132
	K247R	35.7 (1.1)	56 (1)	125
	E244D	37.8 (1.0)	55 (1)	133
$+Ca^{2+}$	WT	38.7 (1.1)	55 (1)	135
	K247R	36.3 (1.0)	51 (1)	127
	E244D	36.8 (1.0)	55 (1)	129

^a Extrapolated values of R_g to $c=0$ in Figure 2. The values in parenthesis are the standard deviations.

^b Calculated from the extrapolated values of $I(0)/c$ to $c=0$ in Figure 2. The value of BSA was used as a standard, employing the M. W. of BSA is 66 kDa. The values in parenthesis are the standard deviations.

Eq. 2, were less than 2.0. To cross-validate the model-data agreement, χ^2_{free} was evaluated against the models obtained [29]. All the models obtained were found to have the χ^2_{free} values less than 1.73, which is less than that accepted for xylanase ($\chi^2_{free}=1.86$; PDB accession number 1HR2) [29]. The models obtained here are thus acceptable. The ensembles of the models obtained provide a measure of the distributions of the possible conformations of the Tn core domain. Figure 5 shows a gallery of the models obtained. The 100 models with the lowest residuals are shown for each sample. The distributions of the models appear to be different between the $-Ca^{2+}$ and $+Ca^{2+}$ states, as well as between WT and the mutants. The averaged scattering curves and the corresponding $p(r)$ functions calculated from these best 100 models are shown as solid curves in Figure 4.

The radius of gyration

Table 2 shows a summary of the averages and the sample standard deviations of the R_g of the whole molecule and each

subunit, calculated from the 1000 models obtained. The average R_g values of the whole molecule fall within a range of one standard deviation of the experimental R_g values. The sets of the R_g values of the models were subjected to the statistical test by the Steel-Dwass method [30,31]. This test is a non-parametric test that can compare multiple data sets simultaneously, and thus applicable to data sets that do not follow normal distributions. The Steel-Dwass test showed that the differences in the average R_g values between the $-Ca^{2+}$ and $+Ca^{2+}$ states are statistically significant at the 95% confidence level. Statistically significant differences are also observed between WT and the mutants. As indicated by the bridges with an asterisk in Table 2, in the $-Ca^{2+}$ state, the R_g of each subunit of K247R is different from that of WT and E244D, whereas the difference between WT and E244D is only in the R_g of the whole molecule. On the other hand, in the $+Ca^{2+}$ state, the values of TnC and TnT are different between WT, K247R, and E244D. The effects of the mutations thus appear to be more significant in K247R than in E244D. Note that the R_g of TnC was found to be between 23.0 Å and 24.5 Å as shown in Table 2. These values are similar to those found for TnC in solution (22.6 Å–27.8 Å) [32–34] and those calculated from the crystal structures of isolated TnC [35–37] using the program CRY SOL without contribution of a hydration shell (22.8 Å–23.2 Å). On the other hand, the R_g of TnC in the crystal structure of the hcTn core domain was calculated to be 19.4 Å using CRY SOL as above. This difference in the R_g values implies that TnC in the Tn core domain in solution adopts more elongated dumbbell-like structures than in crystals.

Characterization of the positions of the movable regions in the Tn core domain

The structure of TnC was characterized by calculating the distribution of the position of the center of gravity of the

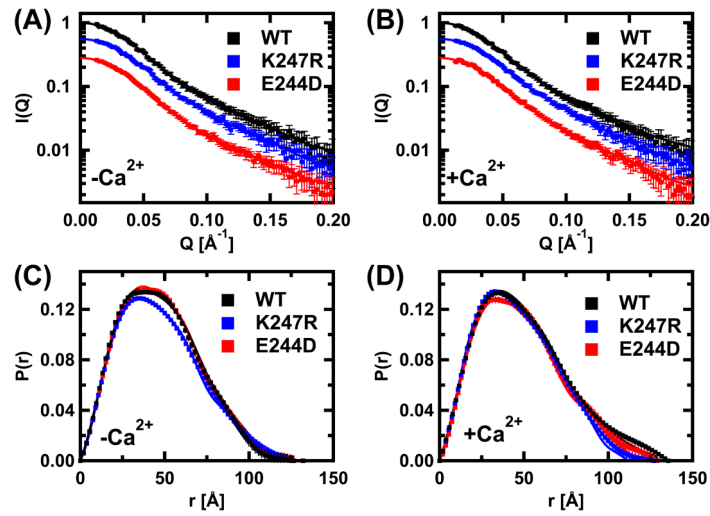


Figure 4 Examples of the small-angle X-ray scattering curves and the pair-distance distribution functions $p(r)$. The extrapolated curves to zero protein concentration of WT, K247R, and E244D in (A) the $-Ca^{2+}$ state and (B) the $+Ca^{2+}$ state are shown by filled squares. The curves are scaled so that the intensity extrapolated to $Q=0$ is unity, but displaced vertically for clarity. Solid lines are the average of the calculated scattering curves of the best 100 models with the lowest residuals to the experimental curves. The panels (C) and (D) show the $p(r)$ functions of WT, K247R, and E244D in the $-Ca^{2+}$ state and the $+Ca^{2+}$ state, respectively. The experimental $p(r)$ functions are shown by filled squares. Those calculated from the best 100 models are shown by solid lines.

N-lobe (TnC_{N-lobe}) relative to that of the C-lobe. The positions of other movable regions, $TnT_{183-223}$, $TnT_{272-288}$, TnI_{31-42} , and $TnI_{137-210}$ were characterized by the positions of the centers of gravity of these regions relative to that of the whole molecule. The parameters for these relative positions were described using the polar coordinate system shown in Figure 6 (the radial distance L , the polar angle θ , and the azimuthal angle ϕ). Figure 7 shows the distributions of these parameter values, which are also summarized in Table 3.

The Steel-Dwass test showed that the differences in the average values of L and θ of TnC_{N-lobe} between the $-Ca^{2+}$ and $+Ca^{2+}$ states in each sample are statistically significant. These differences indicate that by binding of Ca^{2+} , TnC is elongated by about 1–2 Å and its relative orientation is changed. These changes occur regardless of the mutations. The difference in L between WT, K247R, and E244D is also statistically significant, indicating that the relative position of the N-lobe of TnC is different between WT, K247R, and E244D.

Regarding the other movable regions, the most significant differences between WT, K247R, and E244D are in the parameter L for $TnT_{183-223}$ both in the $-Ca^{2+}$ and $+Ca^{2+}$ states. This indicates that by the mutations, the position of the region $TnT_{183-223}$ becomes closer to the center of gravity of the whole molecule. Although the effects are smaller than on $TnT_{183-223}$, in K247R, the L values of other regions including $TnT_{272-288}$ are also different from WT, suggesting that the mutation also affects the positions of these regions. It is thus concluded that the mutations change the distributions of the conformations of the molecule so that the flexible regions, in particular the region $TnT_{183-223}$, become close to the central region of the Tn core domain.

The differences were also observed between the $-Ca^{2+}$ and $+Ca^{2+}$ states. In addition to the differences in the parameters for $TnI_{137-210}$ due to the constraint that the switch helix in TnI binds to TnC in the $+Ca^{2+}$ state [38,39], the differences in the average L values of the regions $TnT_{183-223}$ and $TnT_{272-288}$ were found to be statistically significant by the Steel-Dwass test. This implies that the conformational changes in these regions are involved with the regulatory mechanism.

Discussion

Here, the overall shape changes of the Tn core domain induced by the mutations in TnT were detected by the differences in the R_g and the D_{max} evaluated from the SAXS measurements. Further analysis of the scattering curves with the aid of model calculation detected the conformational changes particularly in TnT by the mutations. The model calculations, from which these results were obtained, were based on the assumptions on the positions and the number of the pivot points and on the structures of the complemented regions. Choice of the pivot points was based on the inspection of the crystal structures of the Tn core domains as described in the Materials and Methods. This choice is also supported by hydrogen-deuterium exchange-mass spectroscopy studies of the hcTn core domain [40,41], which showed that the central region in the IT arm forms a very stable structure whereas the N- and C-terminal regions in TnI and TnT and the linker region between the N- and C-lobes of TnC are highly flexible. The pivot points employed in the present study are located near the ends in these flexible regions. Regarding other assumptions above, additional model

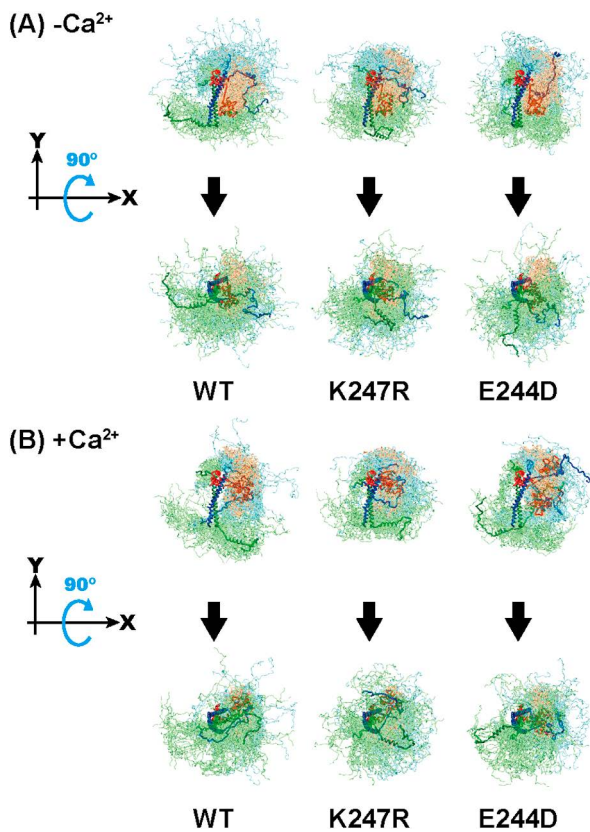


Figure 5 Gallery of examples of the models of the Tn core domain in (A) the $-Ca^{2+}$ state and (B) the $+Ca^{2+}$ state. Superposition of the 100 models with the lowest residuals is shown. TnC, TnI, and TnT in the models are highlighted in orange, sky blue, and green, respectively. The models shown in thick lines, TnC, TnI, and TnT of which are highlighted in red, blue, and forest green, respectively, are the “best” models among the 1000 models obtained. Note that since multiple models have the same lowest χ^2 values in each structural state, one of these “best” models are shown as an example. The views from two different directions are shown: In the lower part of each panel, shown are the models viewed from the direction rotated 90 degrees around the X-axis from that in the upper part. The diagram is drawn using UCSF Chimera.

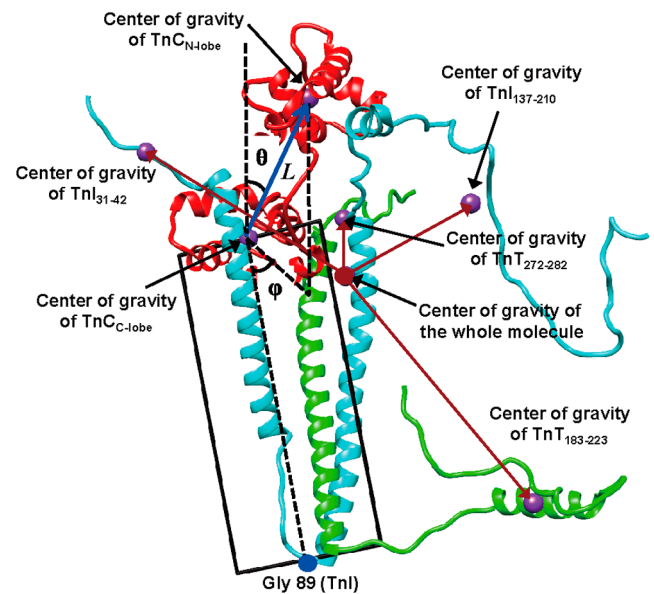


Figure 6 Schematic representation of the parameters defining the centers of gravity of the movable regions. The polar coordinates (L , θ , ϕ) defining the vector from the center of gravity of the C-lobe of TnC to that of the N-lobe of TnC are shown as an example. These coordinates are described in the local coordinate system defined as follows. The origin of the original coordinate system describing the structure is translationally moved to the center of gravity of the C-lobe of TnC. A plane containing the vector from the center of gravity of the C-lobe of TnC to Gly⁸⁹ of TnI and the Y-axis is then defined. In this plane, the vector from the center of gravity of the C-lobe of TnC to Gly⁸⁹ of TnI and the vector perpendicular to it are defined as the new X-axis and the new Y-axis, respectively. The plane containing the new X- and Y-axes is roughly parallel to the plane containing the axis of the coiled-coil formed by the residues 90–137 of TnI and the residues 226–272 of TnT. The coordinates describing the centers of gravity of other regions are defined by translating the origin of the coordinate system defined to the center of gravity of the whole molecule. TnC, TnI, and TnT in the model are highlighted in red, cyan, and green, respectively. The diagram is drawn using UCSF Chimera.

Table 2 Summary of radii of gyration of models

		R_g (whole) (Å)	R_g (TnC) (Å)	R_g (TnT) (Å)	R_g (TnI) (Å)
$-Ca^{2+}$	WT	38.1 (0.3)	23.8 (1.9)	35.9 (4.0)	36.1 (3.9)
	K247R	* [36.5 (0.2)] *	* [23.0 (2.1)] *	* [33.9 (3.9)] *	* [34.8 (3.5)] *
	E244D	* [37.7 (0.3)] *	* [23.9 (1.7)] *	* [35.8 (4.2)] *	* [35.8 (3.7)] *
$+Ca^{2+}$	WT	38.4 (0.3)	24.5 (1.6)	38.7 (5.2)	33.9 (3.8)
	K247R	* [35.8 (0.2)] *	* [23.7 (1.9)] *	* [35.1 (4.1)] *	* [32.8 (2.8)] *
	E244D	* [37.3 (0.3)] *	* [24.1 (1.6)] *	* [37.1 (4.9)] *	* [33.9 (3.4)] *

The values in parenthesis indicate the sample standard deviations.

The bars with an asterisk indicate the difference in the two values bridged by this bar is statistically significant at the 95% confidence level by the Steel-Dwass test.

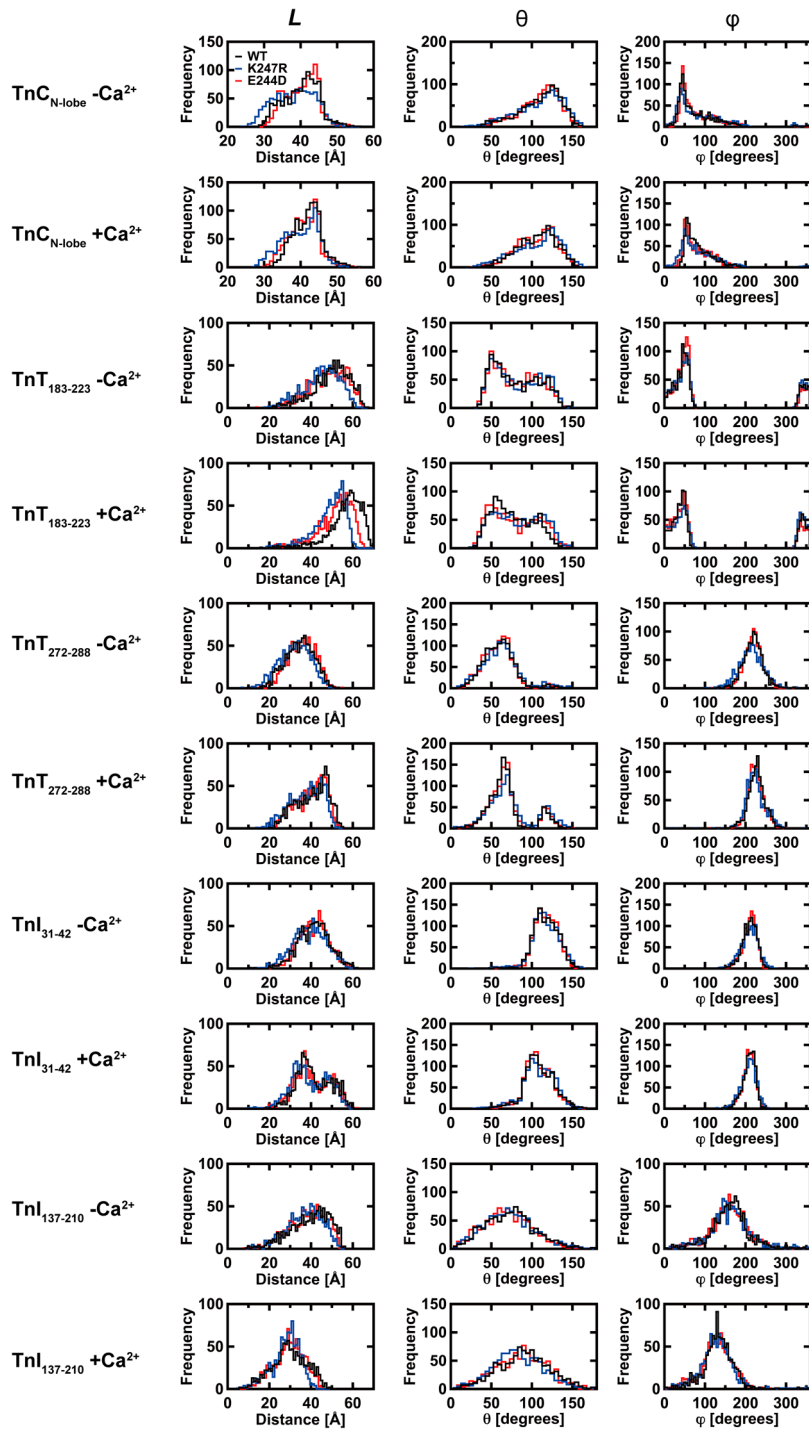


Figure 7 Summary of the distributions of the parameters describing the positions of the movable regions. The parameters for the centers of gravity of the N-lobe of TnC (TnC_{N-lobe}) were calculated relative to the center of gravity of the C-lobe of TnC, and those for the centers of gravity of the regions $TnT_{183-223}$, $TnT_{272-288}$, TnI_{31-42} , and $TnI_{137-210}$ were calculated relative to the center of gravity of the whole molecule. Histograms of frequencies in 1000 models are shown. Solid lines in black, blue, and red are the histograms of WT, K247R, and E244D, respectively.

calculations showed that the changes in the number of the pivot points and in the structures of the complemented regions do not affect the main conclusion of this study that the mutations induce the conformational changes in the N- and

C- terminal regions of TnT, as described in the Supplemental Material. Our modeling results are thus not biased by the assumptions in the model calculation.

An additional constraint that the R_g of the models was

Table 3 Summary of the parameters describing the positions of the movable regions of TnC, TnT, and TnI

		L (Å)	θ (degrees)	φ (degrees)
TnC_{N-lobe}				
-Ca ²⁺	WT	* [40.1 (4.8)	110 (26)	77 (51)
	K247R	* [38.1 (5.5)	109 (29)	86 (64)
	E244D	* [40.2 (4.3)	109 (27)	77 (45)
+Ca ²⁺	WT	* [41.8 (3.9)	106 (24)	* [83 (35)
	K247R	* [39.8 (4.9)	106 (31)	* [84 (48)
	E244D	* [40.9 (4.1)	105 (28)	82 (37)
TnT₁₈₃₋₂₂₃				
-Ca ²⁺	WT	* [49.6 (8.8)	79 (30)	112 (131)
	K247R	* [44.9 (8.7)	81 (31)	118 (134)
	E244D	* [48.1 (9.0)	80 (27)	100 (119)
+Ca ²⁺	WT	* [56.6 (8.1)	* [76 (27)	125 (140)
	K247R	* [48.7 (7.9)	* [82 (31)	* [143 (147)
	E244D	* [51.4 (8.5)	* [78 (30)	* [111 (133)
TnT₂₇₂₋₂₈₈				
-Ca ²⁺	WT	* [34.4 (6.8)	59 (21)	* [218 (28)
	K247R	* [32.0 (7.4)	61 (24)	* [213 (37)
	E244D	* [35.2 (6.7)	59 (20)	* [218 (30)
+Ca ²⁺	WT	* [40.5 (7.6)	* [69 (25)	* [226 (29)
	K247R	* [37.7 (7.7)	* [74 (31)	* [224 (28)
	E244D	* [40.0 (7.2)	* [70 (27)	* [225 (22)
TnI₃₁₋₄₂				
-Ca ²⁺	WT	* [41.3 (7.5)	117 (17)	209 (26)
	K247R	* [39.2 (8.1)	116 (22)	209 (24)
	E244D	* [41.3 (6.9)	117 (16)	209 (26)
+Ca ²⁺	WT	* [41.4 (8.1)	108 (22)	208 (22)
	K247R	* [39.3 (8.8)	108 (22)	206 (27)
	E244D	* [40.7 (8.4)	108 (17)	208 (18)
TnI₁₃₇₋₂₁₀				
-Ca ²⁺	WT	* [39.3 (9.5)	73 (30)	160 (48)
	K247R	* [36.8 (8.5)	71 (33)	161 (52)
	E244D	* [38.0 (8.9)	69 (31)	158 (49)
+Ca ²⁺	WT	* [29.5 (8.4)	* [89 (33)	* [132 (40)
	K247R	* [27.8 (6.8)	* [82 (32)	* [128 (43)
	E244D	* [29.4 (7.3)	* [86 (33)	131 (43)

The model shown in Figure 1 was used as a starting model.

The values in parenthesis indicate the sample standard deviations.

The bars with an asterisk indicate the difference in the two values bridged by this bar is statistically significant at the 95% confidence level by the Steel-Dwass test.

within two standard deviation ranges of the experimental values was introduced to facilitate the convergence of the search. Test calculations showed that the searches without

this additional constraint provide similar ensembles of the structures (data not shown). Thus, this constraint did not distort the results obtained here. Moreover, this constraint is

a reasonable assumption: in a study that the SAXS curves are analyzed as an average of the curves of the snapshots of the structures during the molecular dynamics simulation in an equilibrium state [42], most of the R_g values during the trajectory of 150 nsec are shown to be within two standard deviation range around the experimental R_g value. The ensembles of the structures obtained here thus provide a reasonable measure of the distribution of the possible conformations of the Tn core domain.

Another concern on our model calculations is that each model obtained by our model calculation represents only one of the possible conformations that the Tn core domain can adopt in solution. A possibility of coexistence of multiple conformations is not taken into consideration. To verify if the coexistence of multiple conformations affects the modeling results, we carried out alternative model calculations using the EOM, which takes account of the coexistence of multiple conformations [21]. In the EOM, a set of protein conformers, the average scattering curve of which is fit well with the experimental scattering curve, is selected from a pool of a large number of conformers, based on the genetic algorithm. A representative set of the obtained models by EOM is shown in Figure S4 in the Supplemental Material. The obtained EOM ensembles consist of 3–5 conformers in each state. The parameters corresponding to those shown in Figure 7 for the original models were calculated for each conformer, and comparison of these parameters are shown in Figure S5 in the Supplemental Material. It is shown that the parameters of the EOM models fall within the distribution of the parameters of the original models. Another five independent EOM runs gave the similar results. In particular, the parameter L of $\text{TnT}_{183-223}$ in the $+\text{Ca}^{2+}$ state, which were averaged over the total six independent EOM runs, are found to be 53.3 Å, 52.7 Å, and 51.2 Å for WT, K247R, and E244D, respectively, and the parameter L of $\text{TnT}_{272-288}$ in the $+\text{Ca}^{2+}$ state are 45.4 Å, 41.5 Å, and 42.7 Å for WT, K247R, and E244D, respectively. These results again suggest that the N- and C-terminal regions of TnT tend to be closer to the center of gravity of the whole molecule in the mutants than in WT, supporting the main findings obtained from our model calculation.

This consistency should not be mere coincidence. In cases of intrinsically disordered proteins or multidomain proteins with long flexible linkers, they have high degree of conformational freedom. Structural analysis of these highly flexible proteins would necessarily require to take coexistence of the multiple conformations into account: intrinsically disordered proteins such as α -synuclein, for example, have been modeled as an ensemble of random coils [43], and the structural analysis of ribosomal protein L12, where its two domains are connected with a long flexible linker of 20 residues, has also been carried out based on an ensemble of many coexisting conformers [44]. However, unlike these proteins, about 70% of the residues in the Tn core domain are in well-folded regions. Furthermore, the length of the

linker between the N- and C-lobes of TnC is less than 10 residues. Thus, the degree of conformational freedom of the Tn core domain would be significantly less than that of the proteins mentioned above. Our results that the EOM ensembles obtained for the Tn core domain consist of only 3–5 conformers whereas the EOM ensembles for intrinsically disordered proteins usually consist of as many as 10–20 conformers due to their high flexibility [45] also suggest that flexibility of the Tn core domain is much lower than that of intrinsically disordered proteins. Due to this structural property of the Tn core domain, our model calculation without considering coexistence of the multiple conformations gave the similar results to the EOM. Comparison of the results of our modeling with those obtained by EOM demonstrates that our modeling method is valid for this kind of system.

Our model calculation showed that TnC adopts an elongated dumbbell structure whether the mutations are introduced or not. This elongated dumbbell structure of TnC in the hcTn core domain is consistent with the results of the SANS and SAXS study of the csTn core domain [15]. The elongated dumbbell structure of TnC was also observed for cardiac TnC within the thin filament by SANS [14]. The compact structure of TnC in the crystals of the hcTn core domain is thus likely to be distorted by crystallographic contacts. In this regard, it is noted that in the crystal structure of the csTn core domain, TnC, the N-lobe of which has few crystallographic contacts, adopts an elongated structure [23]. It was also shown that in the $+\text{Ca}^{2+}$ state, this dumbbell structure is elongated further and the orientational change occurs. This is also consistent with the observations for TnC within the thin filament by SANS [14] and neutron fiber diffraction [46]. The orientational change of TnC was also reported for TnC in skeletal muscle [47]. In addition to the conformational change in the region $\text{TnI}_{137-210}$ by binding of Ca^{2+} , which is naturally observed because of the constraint on the model calculation, the conformational changes by binding of Ca^{2+} are also observed in the regions $\text{TnT}_{183-223}$ and $\text{TnT}_{272-288}$. This implies a direct involvement of these regions with the regulatory mechanism because these regions contain the Tm-binding sites [48–53].

The earlier SANS study using the contrast variation technique on the cardiac Tn core domain in the $+\text{Ca}^{2+}$ state reported the smaller R_g values of the whole molecule as well as TnC than those obtained here (33.1 Å for the whole molecule and 20.1 Å for TnC) [12,13]. The source of this discrepancy is not clear. This discrepancy is, however, partly attributable to the different lengths of the constructs for TnI and TnT used: the residues 1–167 in TnI and those 198–298 in TnT were employed in the earlier SANS study whereas the residues 31–210 in TnI and those 183–288 plus extra 12 residues of the His-tag in TnT are employed in the present study. Another difference is in the solution conditions: whereas our solution conditions contain Mg^{2+} both in the $+\text{Ca}^{2+}$ and $-\text{Ca}^{2+}$ states, Mg^{2+} was not included in the solutions employed in the earlier SANS study. Since the differ-

ent effects of Mg^{2+} and Ca^{2+} on the global structure of TnC have been suggested [54–56], the difference in the R_g of TnC may reflect the difference in the structures between TnC with bound Ca^{2+} (the earlier SANS study) and TnC with bound Ca^{2+}/Mg^{2+} (the present study). This point should thus be explored further in the future.

As for comparison with the structure of skeletal Tn, the R_g of the hcTn core domain obtained here is significantly larger than that of the csTn core domain. For example, the R_g of WT in the $-Ca^{2+}$ state is 38.4 Å (see Table 1) whereas the corresponding value of the csTn core domain is 33.1 Å [15]. Since the constructs and the solution conditions employed are similar to each other (except for the extra His-tag at the N-terminus of TnT), the difference could arise from a genuine difference between cardiac Tn and skeletal Tn. Comparison of the crystal structures of the csTn core domain and the hcTn core domain suggests that cardiac Tn shows more flexibility than skeletal Tn [23]. This increased flexibility in cardiac Tn could allow the molecule to have wider distributions of the conformations than in skeletal Tn, and thereby showing “looser” structures.

The results obtained here show that the mutations induce the changes in the distributions of the conformations of the TnT region: in particular, the significant changes are observed in the region TnT_{183–223}. The changes in the region TnT_{272–288} are also observed though the effects appear to be smaller. The N-terminal region in TnT is responsible for the Tm-binding [48,49], and in particular, the residues 183–223 contain the Tm-binding region [49]. The C-terminal region of TnT, including the residues 272–288, is shown to be involved with regulation of ATPase activity through the interactions with Tm and TnI [57,58]. In cardiac muscles, binding of Tn to Tm through these regions applies the force to the Tn complex. On the other hand, the distribution of the conformations that the Tn complex adopts originates from various *intra*- and *inter*-subunit interactions in the complex. The balance between these internal forces and the external force exerted by the binding to Tm should be the essence of the Tn-Tm interaction that ensures the proper transmission of the Ca^{2+} -binding signal from TnC to the downstream Tm via the N- and C-terminal regions of TnT in WT. Our finding that the mutations change the conformational distribution of the Tn complex then implies that the mutations shift this balance and thereby modulating the Tn-Tm interaction. This modulation of the Tn-Tm interaction is likely to cause the aberration in the regulatory function such that the maximum tension increases without alteration of the Ca^{2+} -sensitivity [7,8].

Acknowledgements

We thank Dr. Fumiko Matsumoto for help in sample preparation and small-angle X-ray scattering experiments. We also thank Dr. Chieko Kimura-Sakiyama, Dr. Kayo Maeda, and Prof. Yuichiro Maéda, for help in sample prepara-

tion. We also thank Dr. Takaaki Hikima for help in small-angle X-ray scattering experiments, and Dr. Hidetoshi Kono for help in model calculations. This work was supported in part by a Grant-in-Aid for Scientific Research (C) (Grant No. 21510236) (to S. F.) and a Grant-in-Aid for Young Scientists (B) (Grant No. 24710255) (to T. M.), from the Japan Society for the Promotion of Science.

Conflicts of Interest

The authors declare that they have no conflict of interest.

Author Contributions

S. F. directed the entire project. S. T. carried out crystal structure analysis and helped the model calculations. T. O. and S. F. carried out the SAXS measurements. T. M. and S. F. carried out the data analysis, the model calculations, and co-wrote the manuscript.

References

- [1] Ebashi, S., Endo, M. & Otsuki, I. Control of muscle contraction. *Q. Rev. Biophys.* **2**, 351–384 (1969).
- [2] Tobacman, L. S. Thin filament-mediated regulation of cardiac contraction. *Annu. Rev. Physiol.* **58**, 447–481 (1996).
- [3] Harada, K. & Morimoto, S. Inherited cardiomyopathies as a troponin disease. *Jpn. J. Physiol.* **54**, 307–318 (2004).
- [4] Li, M. X., Wang, X. & Sykes, B. D. Structural based insights into the role of troponin in cardiac muscle pathophysiology. *J. Muscle Res. Cell. Motil.* **25**, 559–579 (2004).
- [5] Maeda, Y., Nitanaï, Y. & Oda, T. From the crystal structure of troponin to the mechanism of calcium regulation of muscle contraction. *Adv. Exp. Med. Biol.* **592**, 37–46 (2007).
- [6] Takeda, S., Yamashita, A., Maeda, K. & Maéda, Y. Structure of the core domain of human cardiac troponin in the Ca^{2+} -saturated form. *Nature* **424**, 35–41 (2003).
- [7] Yanaga, F., Morimoto, S. & Ohtsuki, I. Ca^{2+} sensitization and potentiation of the maximum level of myofibrillar ATPase activity caused by mutations of troponin T found in familial hypertrophic cardiomyopathy. *J. Biol. Chem.* **274**, 8806–8812 (1999).
- [8] Matsumoto, F., Maeda, K., Chatake, T., Maéda, Y. & Fujiwara, S. Functional aberration of myofibrils by cardiomyopathy-causing mutations in the coiled-coil region of the troponin-core domain. *Biochem. Biophys. Res. Commun.* **382**, 205–209 (2009).
- [9] Olah, G. A., Rokop, S. E., Wang, C. L., Blechner, S. L. & Trehwella, J. Troponin I encompasses an extended troponin C in the Ca^{2+} -bound complex: a small-angle X-ray and neutron scattering study. *Biochemistry* **33**, 8233–8239 (1994).
- [10] Olah, G. A. & Trehwella, J. A model structure of the muscle protein complex $4Ca^{2+}$ -troponin C-troponin I derived from small-angle scattering data: implications for regulation. *Biochemistry* **33**, 12800–12806 (1994).
- [11] Stone, D. B., Timmins, P. A., Schneider, D. K., Krylova, I., Ramos, C. H., Reinach, F. C., *et al.* The effect of regulatory Ca^{2+} on the *in situ* structures of troponin C and troponin I: a neutron scattering study. *J. Mol. Biol.* **281**, 689–704 (1998).
- [12] Heller, W. T., Abusamhadneh, E., Finley, N., Rosevear, P. R. & Trehwella, J. The solution structure of a cardiac troponin

- C-troponin I-troponin T complex shows a somewhat compact troponin C interacting with an extended troponin I-troponin T component. *Biochemistry* **41**, 15654–15663 (2002).
- [13] Heller, W. T., Finley, N. L., Dong, W. J., Timmins, P., Cheung, H. C., Rosevear, P. R., *et al.* Small-angle neutron scattering with contrast variation reveals spatial relationships between the three subunits in the ternary cardiac troponin complex and the effects of troponin I phosphorylation. *Biochemistry* **42**, 7790–7800 (2003).
- [14] Matsumoto, F., Makino, K., Maeda, K., Patzelt, H., Maéda, Y. & Fujiwara, S. Conformational changes of troponin C within the thin filaments detected by neutron scattering. *J. Mol. Biol.* **342**, 1209–1221 (2004).
- [15] King, W. A., Stone, D. B., Timmins, P. A., Narayanan, T., von Brasch, A. A. M., Mendelson, R. A., *et al.* Solution structure of the chicken skeletal muscle troponin complex via small-angle neutron and X-ray scattering. *J. Mol. Biol.* **345**, 797–815 (2005).
- [16] Mertens, H. D. T. & Svergun, D. I. Structural characterization of proteins and complexes using small-angle X-ray solution scattering. *J. Struct. Biol.* **172**, 128–141 (2010).
- [17] Matsumoto, F., Deshimaru, S., Oda, T. & Fujiwara, S. Reconstitution of the muscle thin filament from recombinant troponin components and the native thin filaments. *Anal. Biochem.* **399**, 299–301 (2010).
- [18] Fujisawa, T., Inoue, K., Oka, T., Iwamoto, H., Uruga, T., Kumasaka, T., *et al.* Small-angle X-ray scattering station at the SPring-8 RIKEN beamline. *J. Appl. Crystallogr.* **33**, 797–800 (2000).
- [19] Fujisawa, T., Inoko, Y. & Yagi, N. The use of a Hamamatsu X-ray image intensifier with a cooled CCD as a solution X-ray scattering detector. *J. Synchrotron Radiat.* **6**, 1106–1114 (1999).
- [20] Guinier, A. & Fournet, G. *Small-Angle Scattering of X-Rays* (John Wiley and Sons, Inc, New York, 1955).
- [21] Bernado, P., Mylonas, E., Petoukhov, M. V., Blackledge, M. & Svergun, D. I. Structural characterization of flexible proteins using small-angle X-ray scattering. *J. Am. Chem. Soc.* **129**, 5656–5664 (2007).
- [22] Fernandez-Fuentes, N., Zhai, J. & Fiser, A. ArchPRED: a template based loop structure prediction server. *Nucleic Acids Res.* **34**, W173–W176 (2006).
- [23] Vinogradova, M. V., Stone, D. B., Malanina, G. G., Karatzaferi, C., Cooke, R., Mendelson, R. A., *et al.* Ca²⁺-regulated structural changes in troponin. *Proc. Natl. Acad. Sci. USA* **102**, 5038–5043 (2005).
- [24] Svergun, D., Barberato, C. & Koch, M. H. J. CRYSOLE—a Program to Evaluate X-ray Solution Scattering of Biological Macromolecules from Atomic Coordinates. *J. Appl. Crystallogr.* **28**, 768–773 (1995).
- [25] Jones, G. *Genetic and Evolutionary Algorithms. Encyclopedia of computational chemistry* (John Wiley and Sons Inc., Chichester, 2002).
- [26] Pilz, I. Proteins. in *Small Angle X-ray Scattering* (O. Glatter & O. Kratky eds.), pp. 239–293 (London: Plenum Press, London, 1982).
- [27] Feigin, L. A. & Svergun, D. I. *Structure Analysis by Small-Angle X-Ray and Neutron Scattering* (Plenum Press, New York, 1987).
- [28] Petoukhov, M. V., Konarev, P. V., Kikhney, A. G. & Svergun, D. I. ATSAS 2.1—towards automated and web-supported small-angle scattering data analysis. *J. Appl. Crystallogr.* **40**, s223–s228 (2007).
- [29] Rambo, R. P. & Tainer, J. A. Accurate assessment of mass, models and resolution by small-angle scattering. *Nature* **496**, 477–481 (2013).
- [30] Steel, R. G. D. A Rank Sum Test for Comparing All Pairs of Treatments. *Technometrics* **2**, 197–207 (1960).
- [31] Dwass, M. Some k-sample rank-order tests. in *Contributions to Probability and Statistics* (Olkin, I., Ghurye, S. S., Hoëffding, W., Madow, W. G. & Mann, H. B. eds.), pp. 198–202 (Stanford University Press, 1960).
- [32] Hubbard, S. R., Hodgson, K. O. & Doniach, S. Small-angle x-ray scattering investigation of the solution structure of troponin C. *J. Biol. Chem.* **263**, 4151–4158 (1988).
- [33] Wachtel, E. J., Sverbilova, T., McCubbin, W. D. & Kay, C. M. X-ray-scattering of turkey skeletal-muscle troponin C in solution at low pH. *Biochem. J.* **261**, 1043–1046 (1989).
- [34] Fujisawa, T., Ueki, T. & Iida, S. Structural change of the troponin C molecule upon Ca²⁺ binding measured in solution by the X-ray scattering technique. *J. Biochem.* **105**, 377–383 (1989).
- [35] Herzberg, O. & James, M. N. Structure of the calcium regulatory muscle protein troponin-C at 2.8 Å resolution. *Nature* **313**, 653–659 (1985).
- [36] Sundaralingam, M., Bergstrom, R., Strasburg, G., Rao, S. T., Roychowdhury, P., Greaser, M., *et al.* Molecular structure of troponin C from chicken skeletal muscle at 3-angstrom resolution. *Science* **227**, 945–948 (1985).
- [37] Houdusse, A., Love, M. L., Dominguez, R., Grabarek, Z. & Cohen, C. Structures of four Ca²⁺-bound troponin C at 2.0 Å resolution: further insights into the Ca²⁺-switch in the calmodulin superfamily. *Structure* **5**, 1695–1711 (1997).
- [38] Talbot, J. A. & Hodges, R. S. Synthetic studies on the inhibitory region of rabbit skeletal troponin I. Relationship of amino acid sequence to biological activity. *J. Biol. Chem.* **256**, 2798–2802 (1981).
- [39] Takeda, S., Kobayashi, T., Taniguchi, H., Hayashi, H. & Maéda, Y. Structural and functional domains of the troponin complex revealed by limited digestion. *Eur. J. Biochem.* **246**, 611–617 (1997).
- [40] Kowlessur, D. & Tobacman, L. S. Low temperature dynamic mapping reveals unexpected order and disorder in troponin. *J. Biol. Chem.* **285**, 38978–38986 (2010).
- [41] Kowlessur, D. & Tobacman, L. S. Significance of troponin dynamics for Ca²⁺-mediated regulation of contraction and inherited cardiomyopathy. *J. Biol. Chem.* **287**, 42299–42311 (2012).
- [42] Oroguchi, T., Hashimoto, H., Shimizu, T., Sato, M. & Ikeguchi, M. Intrinsic dynamics of restriction endonuclease EcoO109I studied by molecular dynamics simulations and X-ray scattering data analysis. *Biophys. J.* **96**, 2808–2822 (2009).
- [43] Curtain, C. C., Kirby, N. M., Mertens, H. D. T., Barnham, K. J., Knott, R. B., Masters, C. L., *et al.* Alpha-synuclein oligomers and fibrils originate in two distinct conformer pools: a small angle X-ray scattering and ensemble optimization modelling study. *Mol. Biosyst.* **11**, 190–196 (2015).
- [44] Bernado, P., Modig, K., Grella, P., Svergun, D. I., Tchorzewski, M., Pons, M., *et al.* Structure and dynamics of ribosomal protein L12: an ensemble model based on SAXS and NMR relaxation. *Biophys. J.* **98**, 2374–2382 (2010).
- [45] Tria, G., Mertens, H. D. T., Kachala, M. & Svergun, D. I. Advanced ensemble modelling of flexible macromolecules using X-ray solution scattering. *IUCrJ* **2**, 207–217 (2015).
- [46] Fujiwara, S. & Matsumoto, F. Orientational information of troponin C within the thin filaments obtained by neutron fiber diffraction. *J. Mol. Biol.* **367**, 16–24 (2007).
- [47] Sun, Y. B., Brandmeier, B. & Irving, M. Structural changes in troponin in response to Ca²⁺ and myosin binding to thin filaments during activation of skeletal muscle. *Proc. Natl. Acad. Sci. USA* **103**, 17771–17776 (2006).
- [48] Jha, P. K., Leavis, P. C. & Sarkar, S. Interaction of deletion mutants of troponins I and T: COOH-terminal truncation of

- troponin T abolishes troponin I binding and reduces Ca^{2+} sensitivity of the reconstituted regulatory system. *Biochemistry* **35**, 16573–16580 (1996).
- [49] Jin, J. P. & Chong, S. M. Localization of the two tropomyosin-binding sites of troponin T. *Arch. Biochem. Biophys.* **500**, 144–150 (2010).
- [50] Tanokura, M., Tawada, Y., Ono, A. & Ohtsuki, I. Chymotryptic subfragments of troponin T from rabbit skeletal muscle. Interaction with tropomyosin, troponin I and troponin C. *J. Biochem.* **93**, 331–337 (1983).
- [51] Pearlstone, J. R. & Smillie, L. B. Effects of troponin-I plus-C on the binding of troponin-T and its fragments to alpha-tropomyosin. Ca^{2+} sensitivity and cooperativity. *J. Biol. Chem.* **258**, 2534–2542 (1983).
- [52] Morris, E. P. & Lehrer, S. S. Troponin-tropomyosin interactions. Fluorescence studies of the binding of troponin, troponin T, and chymotryptic troponin T fragments to specifically labeled tropomyosin. *Biochemistry* **23**, 2214–2220 (1984).
- [53] Heeley, D. H. & Smillie, L. B. Interaction of rabbit skeletal muscle troponin-T and F-actin at physiological ionic strength. *Biochemistry* **27**, 8227–8232 (1988).
- [54] Fujisawa, T., Ueki, T. & Iida, S. Structural change of troponin C molecule and its domains upon Ca^{2+} binding in the presence of Mg^{2+} ions measured by a solution X-ray scattering technique. *J. Biochem.* **107**, 343–351 (1990).
- [55] Cheung, H. C., Wang, C. K., Gryczynski, I., Wiczek, W., Laczko, G., Johnson, M. L., *et al.* Distance distributions and anisotropy decays of troponin C and its complex with troponin I. *Biochemistry* **30**, 5238–5247 (1991).
- [56] Badr, M. A., Davidson, M. W. & Chase, P. B. Human Cardiac Troponin C undergoes Global Conformational Changes in Response to Divalent Cation Binding: Solution Studies of Fluorescent Protein Constructs by FRET and Analytical Ultracentrifugation. *Biophys. J.* **104**, 448a (2013).
- [57] Gafurov, B., Fredricksen, S., Cai, A., Brenner, B., Chase, P. B. & Chalovich, J. M. The Delta 14 mutation of human cardiac troponin T enhances ATPase activity and alters the cooperative binding of S1-ADP to regulated actin. *Biochemistry* **43**, 15276–15285 (2004).
- [58] Franklin, A. J., Baxley, T., Kobayashi, T. & Chalovich, J. M. The C-terminus of troponin T is essential for maintaining the inactive state of regulated actin. *Biophys. J.* **102**, 2536–2544 (2012).
- [59] Pettersen, E. F., Goddard, T. D., Huang, C. C., Couch, G. S., Greenblatt, D. M., Meng, E. C., *et al.* UCSF Chimera—a visualization system for exploratory research and analysis. *J. Comput. Chem.* **25**, 1605–1612 (2004).